Journal of Power Sources 672 (2026) 239640

Contents lists available at ScienceDirect

Journal of Power Sources

journal homepage: www.elsevier.com/locate/jpowsour

Bi-hourly EIS-DRT diagnostics over 2650 h benchmark degradation of a commercial SOEC under steam electrolysis, co-electrolysis and reversible operation

Felix Mütter [a],*, Pavle Boškoski [b,c], Hartmuth Schröttner [d,e], Christoph Hochenauer [a], Vanja Subotić [a]

[a] *Institute of Thermal Engineering, Graz University of Technology, Inffeldgasse 25/B, Graz, 8010, Austria*
[b] *Jožef Stefan Institute, Department of Systems and Control, Jamova cesta 39, Ljubljana, SI-1000, Slovenia*
[c] *Faculty of Information Studies, Ljubljanska cesta 31a, Novo mesto, 8000, Slovenia*
[d] *Institute of Electron Microscopy and Nanoanalysis (FELMI), Graz University of Technology, Steyrergasse 17, Graz, 8010, Austria*
[e] *Graz Center for Electron Microscopy (ZFE), Steyrergasse 17, Graz, 8010, Austria*

HIGHLIGHTS

- 2650 h single-cell benchmark across steam, co-electrolysis and EC/FC cycling.
- Bi-hourly EIS with neural DP-DRT inversion enables rapid analysis of 1200+ spectra.
- Degradation dominated by rising ohmic resistance R_s, with modest net R_p changes.
- Co-electrolysis adds low-frequency polarisation that is largely reversible in steam.
- Post-mortem SEM shows fuel-side coarsening and larger voids consistent with R_s rise.

ARTICLE INFO

Keywords:
Solid oxide electrolysis (SOE)
Steam electrolysis
Co-electrolysis
Long-term degradation
Syngas
Electrochemical impedance spectroscopy (EIS)
Distribution of relaxation times (DRT)

ABSTRACT

Long-term durability and operating-mode flexibility are barriers to commercial solid oxide electrolysis (SOE) for hydrogen production and supplying syngas for synthetic-fuel synthesis. We report a high-resolution degradation benchmark of a commercial $4 \times 4\,\text{cm}^2$ electrolyte-supported cell operated for 2650 h under six modes that cover steam electrolysis, co-electrolysis at Fischer–Tropsch-relevant syngas conditions at 300 and $500\,\text{mA}\,\text{cm}^{-2}$, repeated steam electrolysis, and reversible electrolysis and fuel cell cycling at 800 °C and fixed gas flows. Bi-hourly electrochemical impedance spectroscopy (EIS) is analysed using a Deep-Prior Distribution of Relaxation Times (DP-DRT)-derived neural DRT solver that processes more than 1200 spectra within minutes, enabling time-resolved separation of ohmic and polarisation contributions. Performance loss is dominated by an increase in ohmic resistance R_s, while polarisation resistance shows only modest net changes. Co-electrolysis mainly adds a low-frequency polarisation contribution that is largely reversible when returning to steam electrolysis. In late-life steam electrolysis at high steam fraction, accelerated ohmic ageing emerges after substantial cumulative operation. Post-mortem SEM reveals fuel-side microstructural coarsening and larger voids. The combination of a single-cell, single-sequence multi-mode campaign with bi-hourly EIS and consistent DRT-based batch inversion provides a uniquely time-resolved, internally comparable degradation dataset that goes beyond end-point voltage trends and enables mode-specific attribution of ageing contributions.

1. Introduction

Climate change is increasingly recognised as one of the most pressing risks to both human societies and the stability of our ecosystems. Tackling this issue will require not only large and permanent reductions in greenhouse gas emissions but also a rapid expansion of renewable energy and the introduction of alternative energy carriers, particularly hydrogen [1]. For industries that are difficult to decarbonise, such as aviation and the steel industry, renewable-based hydrogen and synthetic e-fuels are considered essential options to help reduce dependency on fossil fuels.

---

* Corresponding author.
E-mail address: felix.muetter@tugraz.at (F. Mütter).

https://doi.org/10.1016/j.jpowsour.2026.239640
Received 22 December 2025; Received in revised form 9 February 2026; Accepted 11 February 2026

One very promising technology to help reduce this dependency is solid oxide electrolysis (SOE). It combines very high system efficiencies, with values higher than 83% based on the lower heating value (LHV), and can co-electrolyse CO_2 and H_2O to produce not only green hydrogen but also syngas for subsequent e-fuel synthesis [2–4]. By appropriately choosing fuel gas composition and utilisation, SOE can deliver syngas with H_2/CO ratios close to 2, which is typical for Fischer–Tropsch (FT) synthesis routes. In this work, FT-relevant syngas conditions are used as an application context, while downstream synthesis and system-level integration are not addressed.

However, for a successful commercialisation of this technology efficiency alone is insufficient. A detailed understanding of how operating parameters influence both performance and durability is equally critical. Such knowledge is necessary to optimise operation and extend system lifetime, thereby minimising the levelized cost of hydrogen and syngas/e-fuel production. Notably, bulk inlet gas composition alone is not sufficient to assess Ni oxidation risk in SOC hydrogen electrodes: while electrolysis operation generally shifts the hydrogen electrode to more reducing conditions under load, local deviations from the nominal gas state (e.g., maldistribution, transient steam spikes, or local re-oxidising events) can still govern whether NiO forms [5].

In our previous work, we systematically investigated SOE stack operation in co-electrolysis on a commercial electrolyte-supported stack and identified how operating parameters affect performance under Fischer–Tropsch relevant syngas conditions [6]. In a subsequent study, we applied a design-of-experiments approach to steam electrolysis and established a same-hardware benchmark between steam and co-electrolysis under matched operating windows [7]. Together, these studies addressed short-term, quasi-steady operation and highlight that a holistic assessment of SOE performance requires not only instantaneous metrics but also a direct comparison of long-term stability in both operating modes under application-relevant gas compositions. Accordingly, the operating window investigated here ($T \approx 800$ °C, $j =$ 0.3–0.5 $\mathrm{A\,cm^{-2}}$, steam-rich and Fischer–Tropsch relevant co-electrolysis feeds) was selected to represent a moderate current density window commonly used in long-term single-cell durability studies rather than to constitute an intentionally accelerated stress test. In particular, $j = 0.3\ \mathrm{A\,cm^{-2}}$ is on the lower end of electrolysis current densities and was included as a less aggressive baseline condition, while $j = 0.5\ \mathrm{A\,cm^{-2}}$ provides a higher-load comparison within the same operating window.

1.1. Literature survey - SOE degradation

Long-term degradation studies on SOE cells and stacks exist for both steam electrolysis and co-electrolysis, but direct comparison is often limited by differences in hardware, operating protocols, diagnostics, and even the definition of the degradation rate. Since voltage drift scales with current density and operating conditions, we report literature degradation rates in $\mathrm{mV\,kh^{-1}}$ together with the applied current density. The full set of benchmark entries used in this work is summarised in Table 3 and Fig. 6.

For steam electrolysis, reported degradation spans from single-digit $\mathrm{mV\,kh^{-1}}$ in long-duration tests on electrolyte-supported cells or stacks to tens of $\mathrm{mV\,kh^{-1}}$ at $\sim 1\,\mathrm{A\,cm^{-2}}$, with performance loss frequently associated with ohmic shifts related to electrolyte conductivity changes and fuel-electrode evolution [8–10]. Under deliberately accelerated operation, substantially higher rates have been observed together with pronounced increases in ohmic and fuel-electrode related losses [11].

For co-electrolysis, fewer long-term datasets are available. Reported degradation ranges from moderate values in stack operation near $0.5\,\mathrm{A\,cm^{-2}}$ to severe degradation at high current density in single cells [12,13]. Studies that compare steam and co-electrolysis on identical hardware report mixed trends, indicating strong condition dependence and, in some cases, additional failure modes such as delamination [14–16].

1.2. Scope of this work

Although these studies provide valuable insights, most did not fully exploit electrochemical diagnostics. In particular, high-time-resolution EIS-DRT analysis has not yet been applied systematically to long-term SOE degradation, largely because parameter selection across large datasets is computationally demanding, error-prone, and time-consuming.

Moreover, many experimental campaigns investigate only a single operating mode per cell or stack, which makes it difficult to disentangle operating mode effects from sample-to-sample variability in manufacturing, contacting, alignment, gas distribution, and gas tightness. In this work, a single commercial $4 \times 4\,\mathrm{cm^2}$ electrolyte supported cell is therefore sequentially operated in six different phases (steam electrolysis, co-electrolysis at two current densities, repeated steam electrolysis, and reversible EC/FC cycling) under unchanged hardware, contacting and gas flows. This single-cell, single-sequence approach avoids confounding from hardware-to-hardware variability (manufacturing, contacting, alignment, gas distribution, and gas tightness) by keeping the hardware unchanged across modes.

To enable systematic DRT analysis of the full EIS dataset, DRT distributions were computed using a neural-network implementation derived from the DP-DRT framework of Liu et al. [17], with minor adaptations described in Appendix.

The main highlights of our work can be summarised as follows:

- High-resolution degradation benchmark of a commercial electrolyte-supported SOEC single cell over 2 650 h under steam electrolysis, co-electrolysis at FT-relevant syngas conditions ($H_2/CO \approx 2$), and reversible EC/FC operation at constant temperature and gas flows, using a single-cell, single-sequence design.
- High-time-resolution EIS interpreted with DRT analysis using a DP-DRT-derived neural solver for rapid batch processing of 1200+ spectra.
- Long-term degradation is strongly dominated by an increase in ohmic resistance R_s, while polarisation losses exhibit only modest net changes. Co-electrolysis mainly introduces a reversible low-frequency polarisation resistance contribution, and reversible EC/FC operation at reduced steam fraction yields the lowest electrolysis-segment degradation rate and partial performance recovery.
- Post-mortem SEM reveals fuel-side microstructural coarsening and larger voids compared to the as-bought reference, consistent with the observed increase in R_s and with contact- and fuel-electrode-related losses as likely contributors to performance decay.

2. Experimental setup

2.1. Cell design and test rig setup

A commercial planar electrolyte-supported cell (ESC) of the NextCell-5 type was purchased from *fuelcellmaterials*. The cell is manufactured by *Nexceris* and has an active area of $4 \times 4\,\mathrm{cm^2}$. It is comprised of a multi-layer fuel electrode with a nickel oxide (NiO-YSZ) electrode layer and a gadolinium-doped ceria based (Ni-GDC) composite layer with a total thickness of 50 μ m. The electrolyte is scandium-stabilised zirconia (ScSZ) with a manufacturer-stated nominal thickness of 150 μ m. The multi-layer air electrode has a total thickness of 50 μ m and consists of a lanthanum strontium manganite (LSM) electrode layer and an LSM-GDC composite layer. Contacting of the fuel and air electrodes is facilitated by Ni- and Pt-meshes, respectively. The cell is operated in co-flow configuration.

The supplier does not disclose the detailed composition of the barrier layers. Qualitative EDX spectra acquired at the marked interlayer regions in the post-mortem cross-section show pronounced Ce peaks on

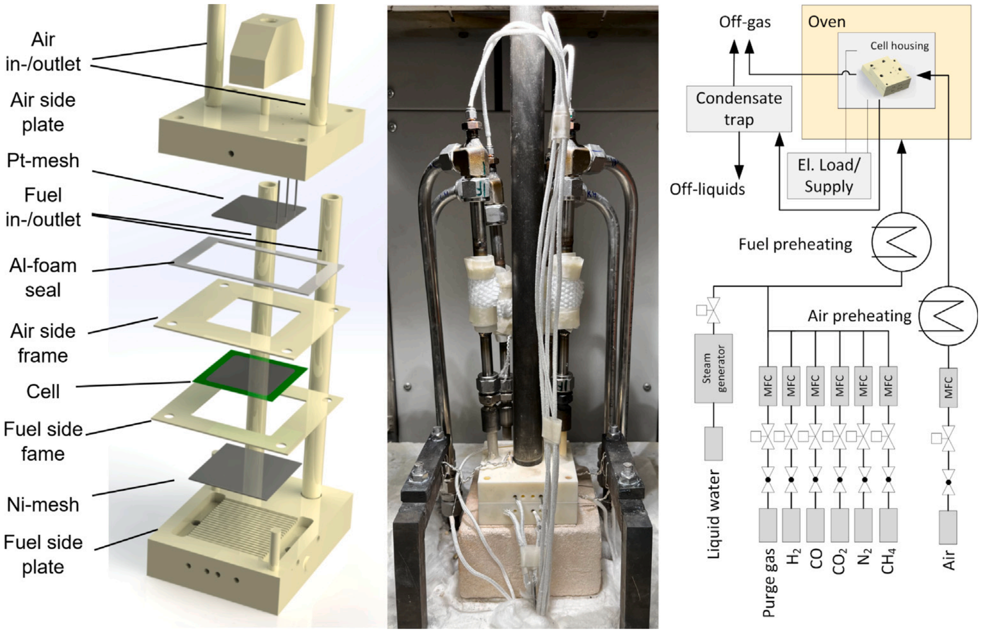

Fig. 1. Schematics of ceramic single cell housing (left), assembled setup in furnace (middle) and schematics of test rig setup (right).

both the fuel and air side. The corresponding spectra are provided in Appendix A.5 (Fig. A.12).

The cell is mounted in a ceramic housing and sealed by alumina foam (air side frame and air side plate) and by a glass powder sealant produced by SCHOTT AG (cell and air side frame). A pneumatic load of 1 kgf/cm^2 is applied via a stainless steel rod. The housing is placed in a furnace and supplied with pre-heated fuel and air gases. Thermal mass flow controllers are used to control the gas flow rates. Steam is supplied by a continuous steam generator fed by deionised water through a SIMDOS® 02 FEM 1.02 dosing pump from ©KNF. A condensation unit downstream of the furnace is used for gas drying. The electric connection of the cell is facilitated through an electronic power supply. The air outlet temperature was measured by a Type N thermocouple and used as the furnace control variable. The air outlet setpoint was set to 805 °C to obtain a housing temperature as close as possible to 800 °C. Unless stated otherwise, the operating temperature reported in this work refers to the housing temperature. The air outlet temperature was selected for control because it provides a stable and reproducible thermal reference for this test rig across different gas compositions and operating modes. Fig. 1 visualises the ceramic single cell housing (left), the assembled setup in the furnace (middle), and the test rig setup (right). Fuel and steam flow rates were chosen such that the reactant conversion rate remained below approximately 10% in all phases. This conservative conversion rate avoids fuel starvation and strong concentration gradients along the flow path and provides stable boundary conditions for the long-term degradation campaign and the high-time-resolution EIS/DRT analysis.

2.2. Analysis methods

Throughout the experiments, gas inlet and outlet compositions, cell housing temperatures on both fuel and air sides, and the cell voltage were continuously monitored. The tested cell is operated in galvanostatic mode and electrochemical impedance spectroscopy (EIS) measurements with optional total harmonic distortion (THD) analysis were performed using a ©Gamry Reference 3000™in combination with a ©Gamry Reference 30K™ booster, which served as power source and sink for electrolysis and fuel cell operation, respectively. EIS measurements were conducted with a 4% AC amplitude superimposed on the DC operating point, using 40 points/decade in the frequency range from 20 kHz to 0.05 Hz with a descending sweep direction. Following the suggestion of Reiner et al. [18], THD was used as an objective criterion to remove outliers. A threshold of 1.5% was imposed on both current and voltage signals, and all frequency points for which the mean THD of either signal exceeded this threshold were discarded for all investigated EIS curves. This global removal enforces an identical frequency grid for all spectra, preventing frequency-dependent selection artefacts and ensuring consistent DRT inversion and time-trend comparability. After THD filtering, the common frequency grid used for all spectra extends up to approximately 10 kHz.

Distribution of relaxation times (DRT). To compute DRT distributions for the full dataset (1248 spectra) within practical time, we employed a neural-network implementation derived from the DP-DRT framework of Liu et al. [17], with minor adaptations for the present measurement grid and joint estimation of the series resistance R_s and a parasitic inductance L (see Appendix A.2 for model details, reconstruction equation, and training objective). The network predicts discrete $G(\tau_k)$ values on a τ-grid matched to the measurement frequencies ($\tau_k = 1/(2\pi f_k)$), enabling impedance reconstruction directly at the measured ω_m points without resampling. On an RTX-class GPU, training over all 1248 spectra required less than 5 min, enabling rapid batch extraction of DRT curves for the time-resolved analyses in this work. The measured spectra exhibit a small high-frequency inductive contribution attributable to leads and cabling. For Nyquist visualisations and for interpreting the high-frequency intercept, we therefore report the inductance-corrected impedance

$$Z_{\mathrm{corr}}(\omega) = Z(\omega) - j\omega L, \tag{1}$$

where L is the parasitic inductance estimated jointly with R_s by the neural DRT solver.

Post-mortem analysis. Post-mortem analysis of the tested cell and an as-bought reference cell was carried out with a Zeiss Ultra 55 scanning electron microscope (SEM) equipped with an EDAX Super Octane EDXS System detector for energy-dispersive X-ray spectroscopy (EDX). For detailed examination of cross-section samples Broad Ion Beam (BIB) polishing was used to prepare the samples.

Table 1

Tested experimental configurations and reactant conversion rates. During phase 5, the reported reactant conversion values correspond to SOEC and SOFC operation, in this order.

ID	Mode	j (mA cm^{-2})	T (°C)	Air (slpm)	Fuel (slpm)	H_2 (slpm)	H_2O (slpm)	CO (slpm)	CO_2 (slpm)	React. conv. (%)
1	Steam el.	300	800	1.2	0.75	0.15	0.60	0	0	5.6
2	Coel	300	800	1.2	0.75	0.10	0.40	0.05	0.20	5.6
3	Coel	500	800	1.2	0.75	0.10	0.40	0.05	0.20	9.3
4	Steam el.	300	800	1.2	0.75	0.15	0.60	0	0	5.6
5	Steam el./FC	300/−150	800	1.2	0.75	0.375	0.375	0	0	8.9/4.5
6	Steam el.	300	800	1.2	0.75	0.15	0.60	0	0	5.6

Table 2

Campaign timeline. Degradation phases refer to the phase IDs in Table 1. Inter phase blocks summarise ramped EIS characterisation performed before and after each degradation phase and any required gas or mode changes between phases.

Seg.	Segment type	Phase ID	t_{start} (h)	t_{end} (h)	Dur. (h)
1	Inter phase block	–	0	22	22
2	Degradation phase	1	22	1022	1000
3	Inter phase block	–	1022	1055	33
4	Degradation phase	2	1055	1455	400
5	Inter phase block	–	1455	1473	18
6	Degradation phase	3	1473	1673	200
7	Inter phase block	–	1673	1701	28
8	Degradation phase	4	1701	2001	300
9	Inter phase block	–	2001	2048	47
10	Degradation phase	5	2048	2312	264
11	Inter phase block	–	2312	2335	23
12	Degradation phase	6	2335	2635	300
13	Inter phase block	–	2635	2650	15
Net galvanostatic operation time (sum of degradation phases)					2464
Non galvanostatic time (sum of inter phase blocks)					186
Gross elapsed campaign time					2650

2.3. Experimental schedule

In the course of this work, six distinct long-term degradation phases were investigated. The campaign comprised steam electrolysis, co-electrolysis at two current densities, a return to the initial steam electrolysis condition, and a reversible EC and FC phase designed to mimic operation strategies under renewable electricity supply. The final phase re-applied the initial steam electrolysis condition to assess time invariance and potential impacts of the reversible operation segment. For all phases, the air and fuel flow rates as well as the temperature were kept constant. Operating conditions and reactant conversion for each phase are summarised in Table 1, while the complete campaign timeline and time accounting are provided in Table 2. Low reactant conversion below 10 percent was intentionally selected to maintain stable boundary conditions and minimise concentration gradients for the bi-hourly EIS and DRT diagnostics across phases. Reactant conversion was calculated from the phase current and inlet reactant molar flow based on Faraday's law using the corresponding degradation phase gas mixture.

Table 2 lists the start and end times of each degradation phase and summarises the inter phase blocks separating consecutive phases.

Before and after each degradation phase, a standardised characterisation sequence was applied to enable direct pre and post comparison. First, a short current ramp was performed with a ramp rate of 10 A min^{-1} to identify a suitable current density window for the subsequent stepwise EIS sequence while remaining within safe operating limits. This current ramp was used exclusively to define the upper current density and thus the number of impedance spectra recorded during the stepwise EIS procedure, and it was not used for the performance evaluation.

Subsequently, a ramped EIS procedure was performed in current density steps of 25 mA cm^{-2}. At each DC setpoint, an impedance spectrum was recorded and the corresponding DC voltage value was logged. The acquisition time per spectrum was approximately 35 min, so that the total duration of one ramped EIS sequence ranged from several hours depending on gas composition, time-under-test, and the resulting number of current density levels that could be measured before reaching the safety limit. The quasi-steady polarisation points reported in this work were obtained from the DC operating points of this ramped EIS sequence.

A voltage safety limit was implemented. If the cell voltage exceeded 1.45 V during the characterisation sequence, the sequence was aborted automatically and the current was set to 0 A.

For the transition between SOFC and SOEC operation during reversible operation (phase 5), mode switching was implemented by reversing the galvanostatic setpoint using a current ramp of 10 A min^{-1}. At 0 A, a pause of 30 s was introduced to record the open-circuit voltage between mode switches.

If a phase change required a gas composition change, gases were changed manually after the post-phase characterisation and before the pre-phase characterisation of the subsequent phase. During phase 5, gas composition was kept constant while only current direction was switched.

3. Results and discussion

This section presents and discusses the results of the 2 650 h multi-mode durability campaign. Voltage and EIS trends are complemented by an ohmic and polarisation resistance decomposition and by DRT and post-mortem SEM/EDX analyses.

3.1. Cell voltage and temperature trends

Fig. 2 summarises the evolution of cell voltage and housing temperatures across all degradation phases. Steam electrolysis, co-electrolysis, and reversible operation are shown in blue, orange, and purple, respectively. Raw voltage traces are plotted in lighter shades, and a 60 s moving average is overlaid to suppress the apparent bandwidth caused by the bi-hourly EIS perturbation. Air- and fuel-side temperatures (pink and green) remained highly stable over the full campaign, with mean values of 801.05 ± 0.53 °C (air side) and 797.75 ± 0.75 °C (fuel side), indicating that the observed voltage drift is not driven by temperature changes.

At the end of each phase, the voltage degradation rate (slope in mV kh^{-1}) is obtained from an ordinary least squares regression over the final 150 h of that phase, and the fitted slope together with its standard error is annotated in Fig. 2. Window selection is not unique and is often handled by excluding an initial equilibration period. In the present campaign, phase durations range from 200 to 1000 h, and the EIS spectra recorded after 24 h (Fig. 3) indicate that relaxation can still be ongoing beyond the first day after a phase change. We therefore exclude the initial 50 h of each phase and use the final 150 h as the longest common late window across all phases, which is constrained by the shortest 200 h phase. This provides a consistent estimate of the stabilised drift while minimising early relaxation effects. Full window degradation rates evaluated over the complete phase durations are additionally provided in Appendix A.1.

The first steam electrolysis phase and the two co-electrolysis phases at 300 and 500 mA cm^{-2} exhibit similar, moderate degradation rates

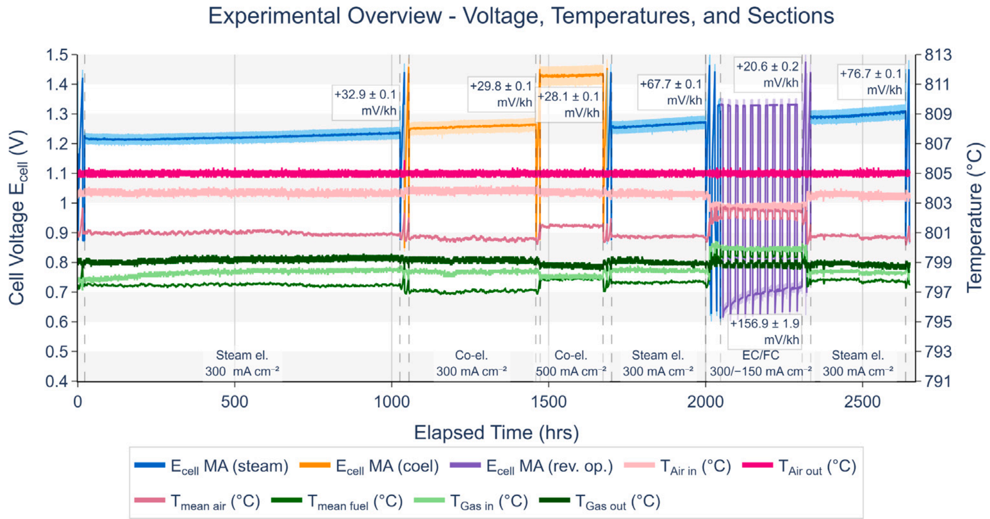

Fig. 2. Overview of cell voltage E_{cell} and housing temperatures over time. The raw E_{cell} signal shows an apparent bandwidth during bi-hourly EIS, which is reduced by the 60 s moving average. End-of-phase degradation rates (OLS slopes over the last 150 h) and their standard errors are annotated. Short voltage fluctuations occur during the EC to FC switchover and reflect switching transients, while comparable fluctuations are not observed during quasi steady ramped EIS characterisations that traverse the same FC current density range.

on the order of 30 mV kh^{-1}, indicating that switching from steam to co-electrolysis and increasing the current density from 300 to 500 mA cm^{-2} only weakly affect the long-term voltage drift. In contrast, the second and third steam electrolysis phases show markedly higher degradation rates of about 70–80 mV kh^{-1}, consistent with a progressive worsening of the dominant degradation mechanism over cumulative operating time. In the reversible EC/FC phase, a separate evaluation of the electrolysis and fuel cell segments shows that the effective degradation rate during electrolysis is substantially lower, around 20 mV kh^{-1}, while the fuel cell voltage even improves slightly over the sequence of cycles. This suggests that, within the investigated operating window, cyclic EC/FC operation does not degrade the cell as strongly as steady-state electrolysis in the other phases and can even recover part of the performance during the initial cycles.

Changing the reactant composition from a high steam fraction (80 %) in the steady steam-electrolysis phases to a lower steam share during reversible operation is therefore associated with a noticeable reduction of the electrolysis degradation rate and partial performance recovery, whereas switching back to 80 % steam continues the trend towards higher degradation. As discussed in more detail in Section 3.7, post-mortem SEM analysis indicates predominantly fuel-side degradation and a comparatively stable air electrode, which is consistent with the fuel-side dominated long-term voltage increase inferred from the global trends in Fig. 2. Local re-oxidation of fuel-side components and contact-related contributions cannot be excluded under the applied conditions, and qualitative indications are provided in Appendix A.5. In addition to the late window slopes over the final 150 h reported in the main text, full window degradation rates evaluated over the complete phase durations are provided in Appendix A.1 in Table A.4.

3.2. Validation of the neural DRT impedance reconstruction

The neural DRT solver was validated by reconstructing $Z(\omega)$ from the recovered $G(\tau)$ together with fitted R_s and inductance and comparing to the measured spectra. Representative spectra from each operation phase show close agreement without visible systematic bias (Appendix, Fig. A.9). Over all frequencies and spectra, the reconstruction error norm $\|\Delta Z\|$ has a median of 0.002 $\Omega\,\text{cm}^2$ (0.251% of the median $|Z|$) and a mean of 0.004 $\Omega\,\text{cm}^2$ (0.580% of the mean $|Z|$).

3.3. Phase-resolved electrochemical performance

Fig. 3 summarises the phase-resolved electrochemical behaviour of the cell. The left panels show stepwise quasi-steady polarisation curves recorded before and after each phase, with the respective phase highlighted and all other phases shown in grey. The polarisation curves in the left panels are derived from the DC operating points of the ramped EIS characterisations recorded before and after each phase. At each current-density level, an impedance spectrum was acquired and the corresponding DC voltage value was logged. Since the acquisition time per spectrum was approximately 35 min, each point represents quasi-steady operation. Dynamic I-V sweeps were not used for the performance evaluation because transient effects after setpoint changes depend on gas composition and operating mode and would introduce mode-dependent bias. Using the ramped EIS operating points ensures consistency between the reported polarisation behaviour and the impedance-based interpretation.

The right panels show the corresponding Nyquist plots at the phase start (grey), after 24 h (light colour), and at the phase end (dark colour), using the same colour scheme as in the preceding figures. The spectra are reconstructed from the DRT distributions and shown as the inductance-corrected impedance Z_{corr} as defined in Eq. (1), using the parasitic inductance L predicted by the neural solver. This ensures that the high-frequency intercept in Fig. 3 is directly consistent with the extracted R_s trends shown in Fig. 4. For the same operating points, the corresponding initial, after ~24 h, and final DRT spectra, along with the extracted LF and HF peak positions and amplitudes used for peak tracking, are provided in Appendix A.6 (Fig. A.13 and Table A.7). Peak assignments are discussed with reference to the process-frequency overview compiled in our previous work, which is intended as a guide rather than a strict classification. Accordingly, the dominant low-frequency (LF) feature (1–100 Hz) is interpreted as primarily reflecting gas-transport and gas-conversion related contributions, while the dominant high-frequency (HF) feature (1–10 kHz) is used as an indicator for faster electrode processes (e.g., charge-transfer and transport contributions commonly reported in the kHz range) [7]. Where multiple local maxima occur within a band, only the dominant maximum is reported for tracking, while secondary features remain visible in the spectra.

Across all phases, the high-frequency intercept shifts gradually to higher resistance, indicating an increasing ohmic contribution. Switching from steam electrolysis to co-electrolysis additionally increases the

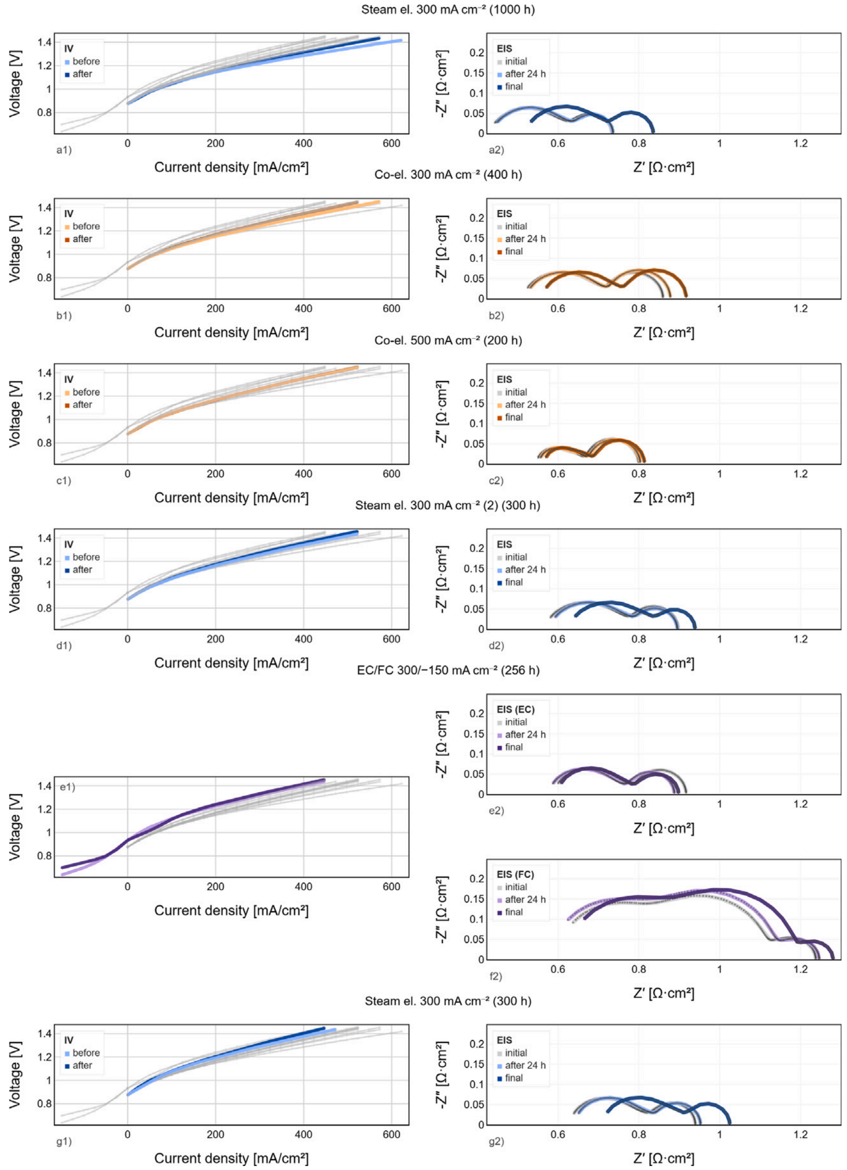

Fig. 3. Left panels show stepwise quasi-steady polarisation curves derived from the DC operating points of the stepwise EIS measurements before and after each phase (coloured), with all other phases shown in grey. Right panels show the corresponding Nyquist plots at phase start (grey), after 24 h (light colour), and at phase end (dark colour). The 24 h spectra indicate incomplete stabilisation. Nyquist plots are shown after series-inductance correction so that the high-frequency intercept corresponds to R_s.

low-frequency diffusion arc, which decreases again after returning to steam electrolysis. The stepwise quasi-steady polarisation curves show corresponding upward shifts after each phase. During reversible EC/FC operation, the high-frequency intercept decreases slightly in the initial cycles and then increases more slowly than in the surrounding steady steam-electrolysis phases. After switching back to 80/20 % H_2O/H_2, the intercept resumes the upward shift observed in the preceding steam phases.

3.4. Decomposition of ohmic and polarisation losses

Fig. 4 shows the ohmic resistance R_s, the polarisation resistance R_p and their sum R_t over all six investigated phases. Markers denote individual EIS spectra, yielding bi-hourly resistance traces over the full campaign. For each phase, as for the voltage trends in Fig. 2, an OLS linear regression is fitted to the last 150 h. The numbers next to the dashed lines denote the corresponding slopes in $\mathrm{m\Omega\,cm^2\,kh^{-1}}$ together with the standard error of each slope. The late-window degradation rates reported here are phase-specific slopes evaluated over the last 150 h of each phase and should not be interpreted as average rates over the full campaign. Phase boundary values and net changes ΔR for each phase, together with full-window rates over the complete phase durations, are provided in Appendix A.1.

A phase-by-phase inspection of the curves highlights how the individual contributions evolve. In the first steam electrolysis period R_s rises at roughly 110.2 $\mathrm{m\Omega\,cm^2\,kh^{-1}}$, while R_p hardly changes. As soon as steam is replaced by the co-electrolysis feed, the R_s slope drops to about 78.7 $\mathrm{m\Omega\,cm^2\,kh^{-1}}$ at 300 $\mathrm{mA\,cm^{-2}}$ and to around 65.7 $\mathrm{m\Omega\,cm^2\,kh^{-1}}$ at 500 $\mathrm{mA\,cm^{-2}}$. In both co-electrolysis phases the total resistance R_t therefore increases slower than in the first steam phase. R_p shows only a weak drift. A slight increase is visible at 300 $\mathrm{mA\,cm^{-2}}$, whereas at 500 $\mathrm{mA\,cm^{-2}}$ there is almost no net change. The diffusion-related contribution in R_p increases when switching from steam to co-electrolysis and decreases again when switching back to steam (phases 2 and 4). This means that the corresponding polarisation contribution can largely be removed by going back to a steam-only feed.

The later steam phases look very different. When the cell returns to 80/20 % H_2O/H_2 after the first three phases, the slope of R_s is markedly higher. It reaches about 169.8 $m\Omega\,cm^2\,kh^{-1}$ in the second steam phase and roughly 232.3 $m\Omega\,cm^2\,kh^{-1}$ in the last one. These are the largest R_s slopes in the whole experiment. R_p starts to increase as well towards the end of the test, but its contribution remains clearly smaller than that of R_s. In other words, the strong long-term deterioration seen in the later steam phases is primarily an ohmic effect.

The reversible EC/FC period sits in between. In this part of the test, both R_s and R_p exhibit a cyclic pattern. Lower resistance values correspond to the SOEC segments, whereas the upper branches in phase 5 are associated with SOFC operation. In the following, only the electrolysis segments are interpreted quantitatively, since the fuel cell branches show larger intra-cycle fluctuations and higher standard errors of the fitted slopes. For the SOEC part of the reversible phase, R_s decreases slightly over the initial cycles and then increases again, but with a much smaller long-term slope than in the surrounding steam phases. The cyclic modulation of R_s and R_p is likely influenced by the small but systematic temperature swings between EC and FC operation visible in Fig. 2. A detailed separation of thermal and electrochemical effects was not attempted in this work.

Overall, Fig. 4 shows that the long-term resistance increase is dominated by R_s, while changes in R_p remain secondary. The diffusion-related additional polarisation contribution observed in co-electrolysis is modest and largely reversible upon returning to steam electrolysis. During reversible EC/FC cycling, the SOEC segments exhibit a noticeably smaller long-term R_s slope than the surrounding 80/20 steam-electrolysis phases, although the underlying trend towards higher ohmic losses is not fully removed.

Full phase degradation rates evaluated over the complete phase durations are additionally provided in Appendix A.1 (Tables A.5 and A.6), alongside the late window slopes over the final 150 h reported in the main text.

3.5. DRT-based time–frequency evolution of polarisation processes

Fig. 5 summarises the time evolution of the DRT peaks within each phase using baseline-subtracted maps. For each phase, the first DRT curve is used as a baseline and subtracted from all subsequent curves of the same phase, so that blue regions indicate a decrease and red regions an increase relative to the phase start.

During the initial steam electrolysis period at 300 $mA\,cm^{-2}$, the DRT distribution remains largely stable over time. The most visible variations are confined to the low-frequency end, which is typically associated with gas-transport or diffusion-related processes, while the mid- and high-frequency regions show only minor changes.

In co-electrolysis at 300 $mA\,cm^{-2}$, an additional low-frequency contribution develops, whereas the mid- and high-frequency ranges remain comparatively unchanged. At 500 $mA\,cm^{-2}$, the overall changes remain limited and the low-frequency feature mainly shifts in characteristic frequency, while the peak intensity shows no systematic increase.

After switching back to steam electrolysis at 300 $mA\,cm^{-2}$, the previously increased low-frequency contribution decreases, confirming the recovery of diffusion-related losses also inferred from Fig. 4. In addition, small changes occur in the high-frequency range around 7 to 10 kHz, which likely reflect minor adjustments in contact-related or other high-frequency processes.

During reversible EC/FC operation, the maps exhibit a cyclic pattern. Relative to the start of the phase, the low-frequency contribution decreases in both EC and FC segments, consistent with reduced diffusion-related losses under the 50/50 % H_2O/H_2 feed. In FC segments, a pronounced increase of a high-frequency feature is observed, whereas the corresponding change during EC operation is weaker. The origin of this high-frequency increase in FC mode is not yet fully understood.

In the final steam electrolysis phase at 300 $mA\,cm^{-2}$, the maps show only moderate evolution, with a slight increase at high frequencies and a small decrease at low frequencies while the overall pattern remains stable. Overall, the DRT maps support the picture that co-electrolysis mainly adds a diffusion-related contribution that is largely reversible upon returning to steam electrolysis, whereas long-term ageing is dominated by the ohmic trend discussed in Section 3.4.

All operating modes were investigated sequentially on the same commercial 4 × 4 cm^2 electrolyte-supported cell in one fixed sequence. Phase-to-phase differences therefore combine operating-mode effects with the accumulated degradation state of the cell, and the benchmark should be interpreted as mode-dependent behaviour along this specific degradation trajectory rather than as statistically generalised separation of mode effects. Within each phase, the bi-hourly EIS and DRT data provide robust trends under constant hardware and boundary conditions, and the decrease of the additional low-frequency contribution upon returning to steam electrolysis supports that the observed mode-dependent signatures are not dominated by a single transition artefact.

3.6. Literature benchmark

Fig. 6 benchmarks the voltage degradation rates from this work against literature data for single cells and stacks in steam and co-electrolysis, plotted as $mV\,kh^{-1}$ versus current density. The purpose of this benchmark is to contextualise whether the degradation rates observed here are comparatively high or low relative to prior reports at similar current density and operating mode. Steam-electrolysis cases are shown as circles, co-electrolysis as squares, and stack data as filled symbols. Studies published within the last decade are highlighted with a green outline. The six phases of this work are marked in red (1) to (6). For the reversible phase the rate refers to the electrolysis segments only.

Across approximately 0.2 to 0.5 $A\,cm^{-2}$, published degradation rates span from a few $mV\,kh^{-1}$ up to about 80 $mV\,kh^{-1}$. All phases of this work fall within this envelope. The initial steam phase (1) lies in the mid-range for single cells at comparable current density. The co-electrolysis phases (2) and (3) are in line with many co-electrolysis reports in Table 3. This supports the resistance-based conclusion that co-electrolysis does not impose a strong additional long-term polarisation contribution relative to steam electrolysis at matched current density. The later steam phases (4) and (6) approach the upper part of the reported range at 300 $mA\,cm^{-2}$. This is consistent with accelerated ohmic ageing and qualitative indications of fuel-side degradation in Appendix A.5 and Fig. A.11, yet the rates remain within the spread reported for commercial-type cells tested under comparable conditions. The reversible EC/FC phase (5) yields one of the lowest rates in this dataset and is competitive with cycling studies at similar current density.

Literature degradation rates are defined heterogeneously, for example via net end to start voltage change, ASR-derived rates, and in some cases reversible-operation data. In contrast, the present work uses consistent late-window slopes over the last 150 h of each phase. The benchmark should therefore be interpreted as indicative positioning rather than a strictly standardised one-to-one comparison. Within this context, the best-performing phases, including co-electrolysis and reversible operation, fall in the lower to mid portion of the literature spread. The harsher late-life steam phases approach but do not exceed the upper bound, consistent with the known sensitivity of Ni-based fuel electrodes to operating conditions and microstructural details.

3.7. Post-mortem SEM analysis

Post-mortem surface SEM was performed on the air and fuel electrodes of the tested cell and on an as-received green reference cell. Representative surface views at the inlet, middle and outlet regions are

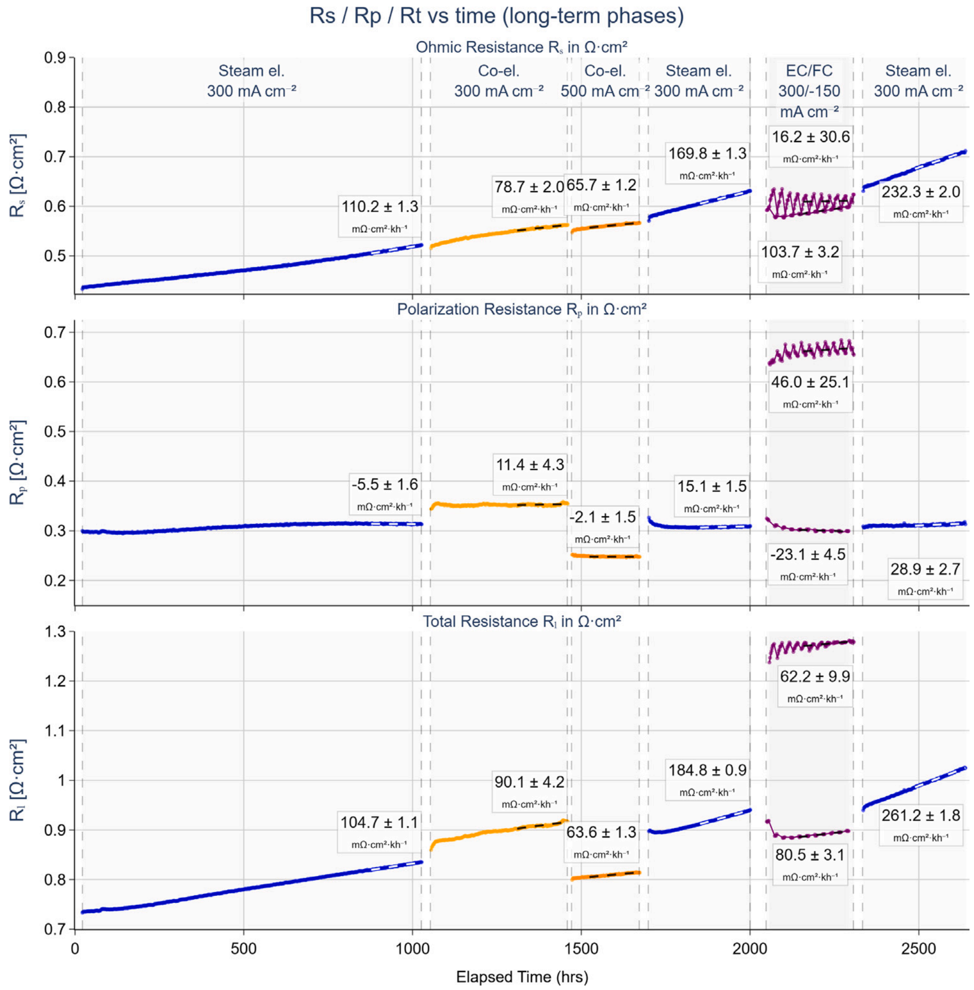

Fig. 4. Ohmic (R_s), polarisation (R_p) and total resistance (R_t) versus operating time for all six phases. Symbols and solid lines show DRT-derived resistances. Shaded regions and labels indicate the operating modes. Dashed lines are linear fits over the last 150 h of each phase, and annotations report degradation rates in $m\Omega\,\mathrm{cm}^2\,\mathrm{kh}^{-1}$ together with the standard error of the fitted slope.

compared in Fig. 7. In addition, a cross-section SEM image of the centre was analysed and is shown in Fig. 8.

On the air side (Fig. 7a-d), the LSM-based electrode microstructure after the long-term multi-phase test appears very similar along the flow direction and to the reference. The granular morphology with interconnected grains and necks is preserved, with no significant grain growth visible at 800 °C. The overall porosity and pore-size distribution remain comparable, and no large cracks or extended voids are observed in the inspected regions at this magnification. Within the resolution of these images, the air electrode therefore appears comparatively stable over the course of the investigated operating sequence.

In contrast, the fuel electrode shows clear evidence of morphological evolution compared to the as-received state (Fig. 7e-h). The reference cell was examined in a fully oxidised state, so some morphological differences are expected. Nevertheless, the reference fuel electrode exhibits a significantly finer and much more uniform Ni/YSZ network with smaller, more homogeneous pores. The post-mortem fuel electrode, at all axial positions, as well as in the cross-section image, displays pronounced coarsening of Ni-containing agglomerates and the formation of larger, irregular voids and caverns within the porous backbone. The structure appears significantly less uniform and more heterogeneous in terms of grain size and pore distribution than in the reference. These observations indicate that the fuel electrode has undergone substantial restructuring during operation, involving particle growth and the development of larger voids.

The SEM analysis is limited to selected surface regions of a single cell and does not resolve fine-scale changes throughout the full electrode thickness or current-collector contact region.

The fuel-side microstructural changes are consistent with oxidation-related restructuring and contact degradation under the present steam-rich feeds at conservative fuel utilisation. Because electrolysis polarisation typically supports Ni stability at the hydrogen electrode, the observed fuel-side degradation is more consistent with local departures from the nominal reducing environment, for example local gas inhomogeneity or transient re-oxidation, than with a bulk-chemistry effect of steam fraction alone [5]. EDX spectra at the marked cross-section locations are provided in Appendix as qualitative support for locally oxidised Ni at the analysed locations, see Fig. A.11. This implies that Ni-related degradation remains a relevant risk for the investigated Ni-based fuel electrode and contact design, while the rate and spatial extent of oxidation- and contact-related damage depend on fuel utilisation, flow field, and current density in a given system.

Within the resolution of the cross-section SEM analysis in Fig. 8, no obvious delamination, cracking, or gross morphological alteration of the electrolyte and air-electrode layers was observed. A SEM cross-section of an unreduced reference cell prepared and imaged using the same workflow is provided in the Appendix A.4 (Fig. A.10) to enable direct baseline comparison of the layer stack and microstructure. Subtle microstructural changes, in particular in the porous electrodes, cannot be excluded within the present spatial sampling and the qualitative nature of the comparison.

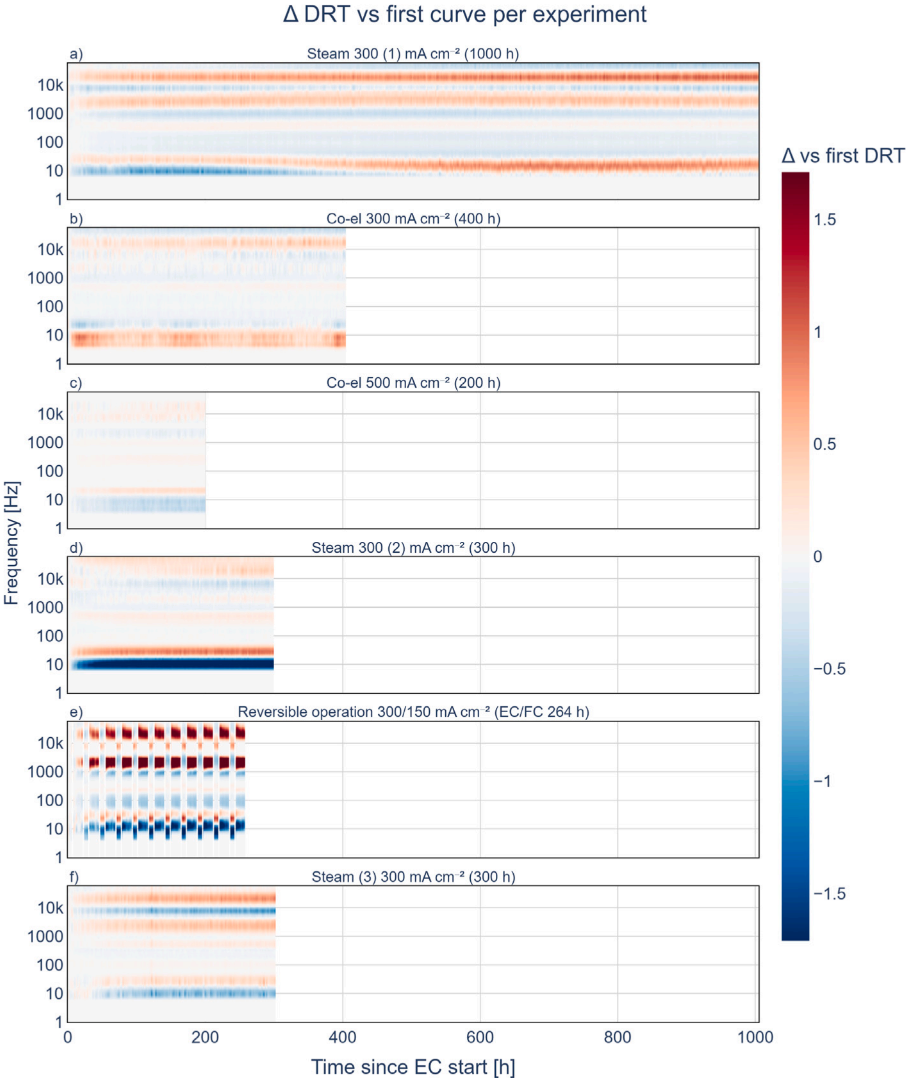

Fig. 5. Baseline-subtracted DRT maps for each phase. Within each phase, the first DRT curve is subtracted from all subsequent curves, where blue indicates decreasing and red increasing peak intensities relative to the phase start. Panels (a) to (f) correspond to steam electrolysis at 300 mA cm^{-2}, co-electrolysis at 300 mA cm^{-2}, co-electrolysis at 500 mA cm^{-2}, steam electrolysis at 300 mA cm^{-2}, reversible EC/FC operation at 300/−150 mA cm^{-2}, and a final steam electrolysis phase at 300 mA cm^{-2}.

4. Conclusion

In this work, a commercial 4 × 4 cm^2 electrolyte-supported solid oxide cell was subjected to a 2 650 h multi-phase degradation campaign comprising steam electrolysis, co-electrolysis at two current densities, and reversible EC/FC operation at constant temperature and gas flows. Bi-hourly EIS measurements were analysed with a neural-network-based DRT framework, enabling high-time-resolution decomposition of voltage degradation into ohmic and polarisation contributions for all six operating phases.

Across the full test, the long-term performance loss was overwhelmingly governed by an increase in ohmic resistance. The polarisation resistance exhibited only modest net changes, with more subtle adjustments of individual high-, mid-, and low-frequency processes over time. Co-electrolysis at 300 and 500 mA cm^{-2} introduced an additional low-frequency polarisation contribution relative to steam electrolysis, but this low-frequency contribution was largely reversible: switching back to steam operation at otherwise unchanged conditions removed most of the added diffusion-related contributions within the subsequent steam-electrolysis phase. Within the investigated current range, increasing the co-electrolysis current density from 300 to 500 mA cm^{-2} did not lead to a substantially higher long-term degradation rate.

The later steam electrolysis phases at high steam fraction exhibited markedly accelerated ohmic ageing at advanced cell age, and this acceleration should be interpreted as condition-dependent behaviour after substantial cumulative operation rather than as an isolated effect of steam fraction alone. In contrast, the reversible EC/FC phase operated at a lower steam fraction yielded one of the lowest electrolysis-segment degradation rates in this study and exhibited partial recovery of the high-frequency intercept during the initial cycles. For this commercial ESC and along the investigated degradation trajectory, late-life high-steam steady-state electrolysis coincided with the strongest acceleration of Rs, whereas co-electrolysis and reversible operation showed lower net electrolysis-segment rates under the tested conditions.

Post-mortem SEM analysis revealed pronounced microstructural changes at the fuel side, with Ni-containing regions showing particle coarsening and larger, irregular voids, while the air electrode remained comparatively stable within the resolution of the measurements. The localisation of these changes on the fuel electrode, together with the observed R_s-dominated ageing and the stronger degradation in high-steam phases, suggests that fuel-electrode microstructural coarsening and contact-related losses are plausible contributors to the observed ohmic degradation, although contributions from other cell components

Table 3
Entries used for the degradation-rate benchmark plot, including operating conditions and inlet gas compositions. Grouped by operation mode (steam, then co-electrolysis) and sorted by degradation rate DR (ascending) within each group. DR denotes voltage degradation rate in mV kh^{-1}. Unless stated otherwise, literature values are based on the net voltage difference between the beginning and end of the reported test. In some cases (as indicated in the notes), the values are derived from ASR or rSOC cycling data and are therefore only approximately comparable to the present single-cell steady-state electrolysis slopes.

Reference	Device	Mode	j [A cm^{-2}]	DR [mV kh^{-1}]	T [°C]	H_2 [%]	H_2O [%]	CO [%]	CO_2 [%]	Notes
[14]	single cell	steam	0.50	5.8	800	20	80	0	0	
[15]	stack	steam	0.30	6.0	760	50	50	0	0	
[10]	stack	steam	0.52	6.4	820	9	80	0	0	N_2 = 11%
[9]	single cell	steam	0.90	7.4	850	25	75	0	0	
[19]	stack	steam	0.50	8.8	800	50	50	0	0	estimated from ASR
[20]	stack	steam	0.50	9.1	700	20	80	0	0	** reversible operation
[15]	stack	steam	0.875	19.0	810	50	50	0	0	
This work (5)	single cell	steam	0.30	20.6	800	50	50	0	0	** reversible operation
[21]	stack	steam	0.30	27.0	750	20	80	0	0	** reversible operation
This work (1)	single cell	steam	0.30	32.9	800	20	80	0	0	
[22]	single cell	steam	1.00	53.0	800	10	90	0	0	
This work (4)	single cell	steam	0.30	67.7	800	20	80	0	0	
This work (6)	single cell	steam	0.30	76.7	800	20	80	0	0	
[16]	single cell	steam	1.00	370.0	800	50	50	0	0	clipped in plot
[14]	single cell	co-el	0.40	3.9	800	13	53	7	27	
[13]	stack	co-el	0.50	5.6	750	10	65	0	25	* cycled
[15]	stack	co-el	0.30	11.5	760	50	25	0	25	
[14]	single cell	co-el	0.40	20.0	800	13	53	7	27	
This work (3)	single cell	co-el	0.50	28.1	800	13	53	7	27	
This work (2)	single cell	co-el	0.30	29.8	800	13	53	7	27	
[14]	single cell	co-el	0.40	133.8	800	13	53	7	27	clipped in plot
[16]	single cell	co-el	1.00	179.0	800	20	40	0	40	clipped in plot
[15]	stack	co-el	0.80	81.6	760	44	33	0	22	clipped in plot

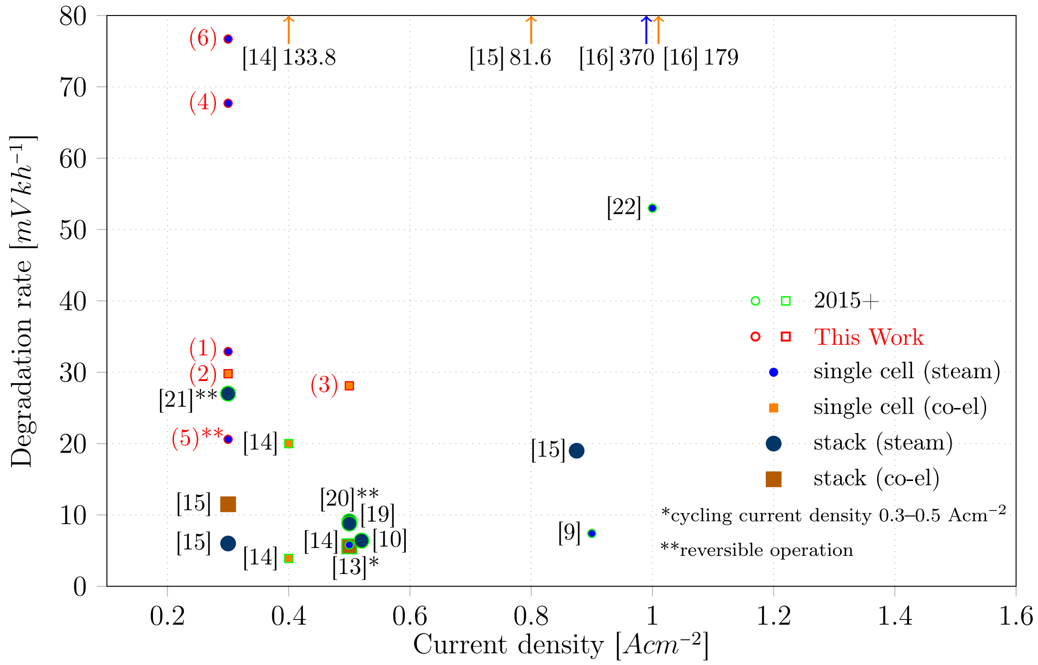

Fig. 6. Literature benchmark of reported voltage degradation rates in **mV kh^{-1}** as a function of current density for single cells and stacks operated in steam electrolysis and co-electrolysis. Values published within the last 10 years are marked with a green outline, and points from *This Work* are highlighted with a red frame. The purpose of this chart is to contextualise the magnitude of the degradation observed here relative to prior studies at comparable current densities and operating modes. Degradation rates from this work correspond to late-window slopes obtained from ordinary least-squares fits over the last 150 h of each phase, whereas many literature values represent average changes over the full reported test duration and in some cases are derived from ASR or reversible-operation metrics. The comparison is therefore indicative rather than strictly one-to-one.

and interfaces cannot be completely excluded. The specific underlying mechanisms, such as local changes in gas composition, mechanical reorganisation at contact interfaces, or other thermochemically driven processes, remain to be clarified.

The DRT analysis in this work used a DP-DRT-derived neural DRT solver as a fast inversion tool for the measured impedance spectra. This enabled a consistent, time-resolved separation of ohmic and diffusion-related contributions across all operating phases, with implementation

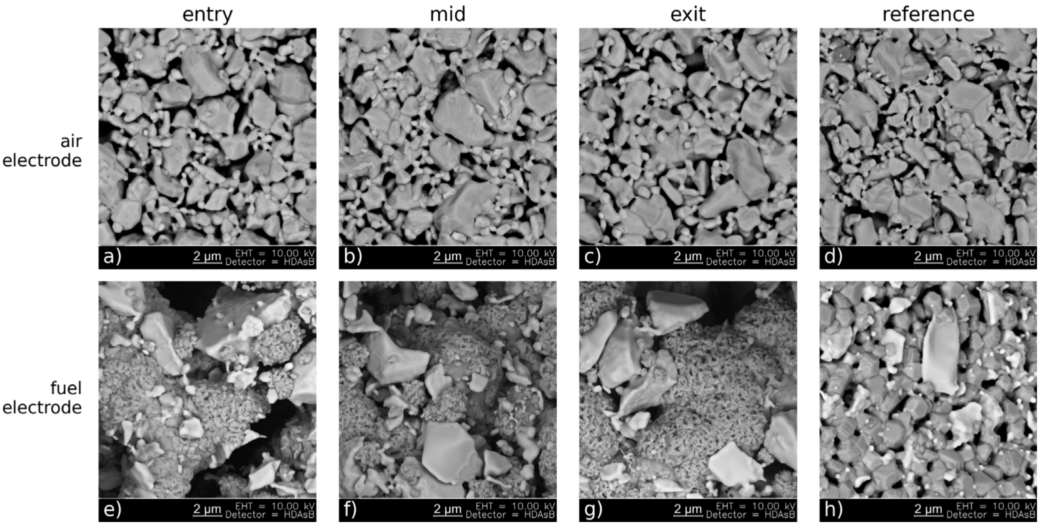

Fig. 7. Post-mortem surface morphology of the air (top row) and fuel (bottom row) electrodes at the inlet (a, e), middle (b, f) and outlet (c, g) of the tested cell, compared with an as-received green reference cell (d, h). All images were recorded at 10 kV with identical magnification (scale bar 2 μ m). The air electrode shows no significant grain growth and remains similar to the reference, whereas the fuel electrode exhibits pronounced particle coarsening and larger, irregular voids compared to the finer, more homogeneous reference morphology.

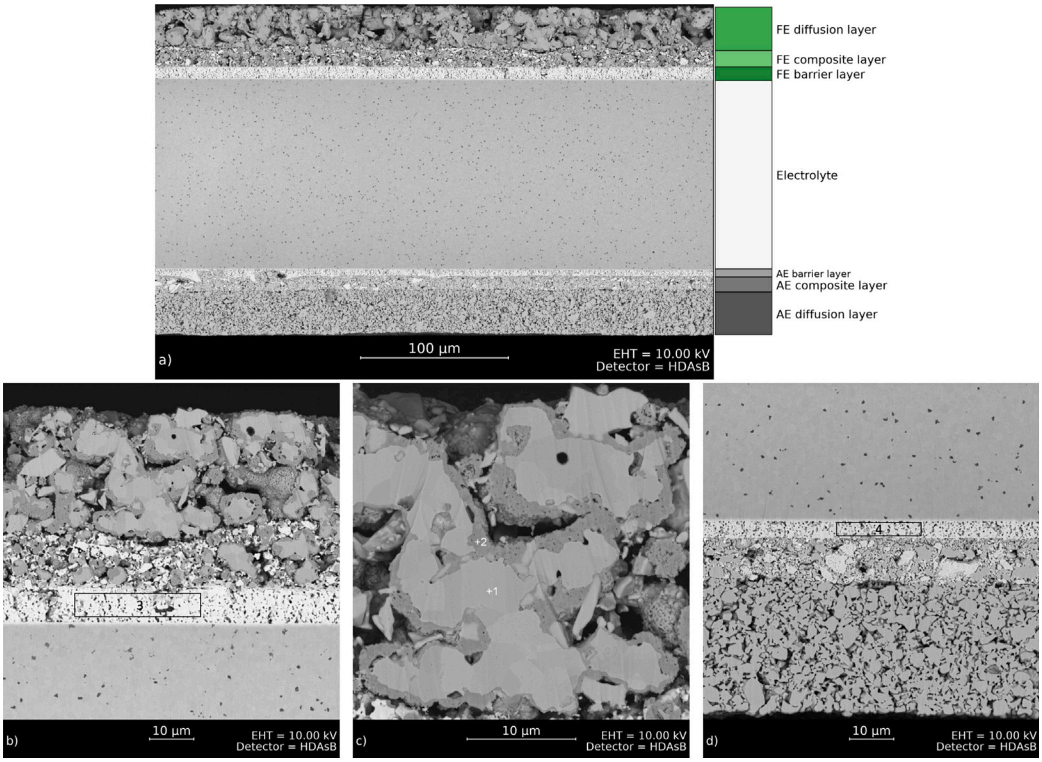

Fig. 8. Post-mortem SEM cross-section of the tested cell. Panel (a) shows the full cross-section with the fuel electrode (top), electrolyte, and air electrode (bottom), including diffusion, composite or functional, and thin barrier layers on both sides. Panels (b) and (c) provide higher-magnification views of the fuel electrode region, revealing pronounced particle coarsening and the formation of larger, irregular voids. Panel (d) shows a higher-magnification view of the air electrode region, which remains comparatively fine and homogeneous with an intact electrode to electrolyte interface. All images were recorded at 10 kV using the HDAsB detector. Scale bars are 100 μ m in (a) and 10 μ m in (b-d). The numbered markers (+1 and +2) in panel (c) and (3 and 4) in panel (b) and (d) indicate EDX measurement locations. The corresponding spectra are provided in Appendix (see Figs. A.11 and A.12). The electrolyte thickness measured on the post-mortem cross-section is approximately 130 μ m, depending on measurement position.

details and reconstruction validation provided in Appendix. While the present analysis is limited to a single cell and one specific operating sequence, the combined use of high-resolution EIS and systematic long-term testing provides a practical route to disentangle degradation contributions and to evaluate SOE operating strategies, including co-electrolysis and reversible operation.

5. Outlook

The present study was limited to a single commercial $4 \times 4\,\mathrm{cm}^2$ electrolyte-supported cell operated continuously for 2 650 h. This design ensures full comparability of the investigated operating modes under identical hardware and boundary conditions, but it does not address statistical variability or potential sequence effects. Repeated long-term experiments with a reversed sequence of operating modes and dedicated steady-state reference runs at the initial gas composition are therefore required to confirm the robustness and generality of the observed R_s-dominated degradation behaviour.

In addition, systematic variation of steam fraction and deliberately imposed gas and pressure transients would help to disentangle the underlying fuel-electrode and contact-related degradation mechanisms. Finally, applying the neural-network-based DRT solver to additional single-cell and stack datasets will be essential to assess its transferability and to further establish high-resolution EIS/DRT diagnostics as a practical tool for evaluating advanced SOE operating strategies.

CRediT authorship contribution statement

Felix Mütter: Writing – review & editing, Writing – original draft, Visualization, Validation, Software, Methodology, Investigation, Formal analysis, Data curation, Conceptualization. **Pavle Boškoski:** Writing – review & editing, Validation, Software, Methodology, Conceptualization. **Hartmuth Schröttner:** Investigation, Data curation. **Christoph Hochenauer:** Resources, Funding acquisition. **Vanja Subotić:** Resources, Funding acquisition.

Declaration of generative AI and AI-assisted technologies in the manuscript preparation process

During the preparation of this work the author(s) used the tool DeepL, in order to improve the readability and flow of the manuscript text. After using these tools the author(s) reviewed and edited the content as needed and take(s) full responsibility for the content of the published article.

Declaration of competing interest

The authors declare that they have no known competing financial interests or personal relationships that could have appeared to influence the work reported in this paper.

Acknowledgements

This work was supported in part by funding from Graz University of Technology, Austria. The authors express sincere gratitude for the support received for the project "Probabilistic and explain- able data-driven modelling of solid-oxide system" jointly financed by the Slovenian Research and Innovation Agency (ARIS) (project number J2-4452) and Austrian Science Fund (FWF). This research was funded in whole, or in part, by the Austrian Science Fund (FWF) [10.55776/I6251]. For the purpose of open access, the author has applied a CC BY public copyright licence to any Author Accepted Manuscript version arising from this submission.

Appendix. Supplementary data

A.1. *Tabular values from degradation trends*

Full window rates are computed from the phase boundary values over the complete phase duration, while late window rates denote the OLS slope over the final 150 h.

A.2. *Neural-network-based DRT reconstruction*

We employed a neural-network implementation derived from the DP-DRT framework of Liu et al. [17] to reconstruct $G(\tau)$ and jointly estimate the series resistance R_s and a parasitic inductance L from the measured impedance spectra. The core model is a fully connected encoder-bottleneck-decoder network with layer sizes $(n_\mathrm{in}, 256, 64, 256, N_\tau)$. Input features are constructed from the real and imaginary parts of the impedance and mapped to discrete DRT values $G(\tau_k)$ defined on a relaxation-time grid $\{\tau_k\}$ matched to the measurement frequency sampling via $\tau_k = 1/(2\pi f_k)$. In this way, the impedance reconstruction is evaluated directly at the measured frequency points ω_m without resampling or interpolation. The covered τ-range therefore follows from the experimental frequency window.

In addition to the DRT branch, two shallow regression heads are attached to the shared encoder. One head processes the real-part channel to predict R_s. The second head processes the imaginary-part channel to predict L. Each head consists of a single hidden layer with 32 units and ReLU activation, followed by a softplus output layer to enforce positivity of R_s and L.

The complex impedance is reconstructed by numerically evaluating the DRT integral using a trapezoidal rule,

$$Z(\omega_m) = R_\mathrm{s} + \sum_k \frac{G(\tau_k)}{1 + \mathrm{j}\,\omega_m \tau_k}\,\Delta \ln \tau + \mathrm{j}\,\omega_m L,$$

and split into real and imaginary parts $Z'(\omega_m)$ and $Z''(\omega_m)$ within the loss function. The training objective is a composite loss combining an adaptive relative L1-type data misfit with a smoothness regularisation term on the DRT:

- *Data misfit* relative L1 deviation between measured and reconstructed impedance, applied jointly to $Z'(\omega_m)$ and $Z''(\omega_m)$
- *Smoothness* mean squared discrete second derivative of $G(\tau_k)$ on the $\ln \tau$-grid, which penalises oscillatory solutions and promotes physically plausible, smooth DRTs

In the present work we use a smoothness weight $\lambda_\mathrm{smooth} = 10^4$, chosen empirically to balance data misfit and regularisation for the scaling of the problem. The absolute value of λ_smooth is implementation dependent due to loss normalisation, impedance scaling, and τ-grid parameterisation. It should not be compared directly to regularisation parameters reported in other DRT frameworks. We note that changing λ_smooth primarily affects the smoothness and peak fragmentation of $G(\tau)$. The time-trends in R_s and the phase-level conclusions reported in this work remain stable within reasonable settings.

All network parameters, including the DRT branch and the R_s and L heads, were optimised jointly using the AdamW optimiser. Training was performed for 10^5 iterations with a cyclic learning-rate schedule in the sense of Smith [23], implemented via a PyTorch `CyclicLR` scheduler with an exponential range policy. We used a minimum learning rate of 5×10^{-7}, a maximum learning rate of 5×10^{-4}, and symmetric up-down half cycles of 5000 iterations, resulting in ten full learning-rate cycles over 10^5 iterations. On an NVIDIA RTX-class GPU with CUDA and an AMD Ryzen 9 7900 CPU, the total training time for a full run over all 1248 spectra was less than 5 min.

Table A.4

Voltage at the phase boundaries from Table 2 with full-window and late-window degradation rates. k^{full} uses the full phase duration, and k^{150} is the OLS slope over the final 150 h (see Fig. 2).

Phase	Mode	t_0 [h]	t_1 [h]	Δt [h]	$U^{(0)}$ [V]	$U^{(1)}$ [V]	ΔU [mV]	k^{full} [mV kh^{-1}]	k^{150}
Steam el. (1) (300 mA cm^{-2})	EC	22	1022	1000	1.222	1.236	14.0	14.000	32.9 ± 0.1
Coel (300 mA cm^{-2})	EC	1055	1455	400	1.246	1.265	19.0	47.500	29.8 ± 0.1
Coel (500 mA cm^{-2})	EC	1473	1673	200	1.429	1.432	3.0	15.000	28.1 ± 0.1
Steam el. (2) (300 mA cm^{-2})	EC	1701	2001	300	1.256	1.291	35.0	116.667	67.7 ± 0.1
EC/FC (300/−150 mA cm^{-2})	EC	2048	2312	264	1.333	1.331	−2.0	−7.576	20.6 ± 0.2
	FC				0.616	0.717	101.0	382.576	156.9 ± 1.9
Steam el. (3) (300 mA cm^{-2})	EC	2335	2635	300	1.283	1.306	23.0	76.667	76.7 ± 0.1

Table A.5

First and last resistance values per phase using the campaign clock from Table 2. For Phase 5, EC and FC are listed separately.

Phase	Mode	t_0 [h]	t_1 [h]	Δt [h]	$R_s^{(0)}$ [mΩ cm^2]	$R_s^{(1)}$ [mΩ cm^2]	ΔR_s [mΩ cm^2]	$R_p^{(0)}$ [mΩ cm^2]	$R_p^{(1)}$ [mΩ cm^2]	ΔR_p [mΩ cm^2]	$R_t^{(0)}$ [mΩ cm^2]	$R_t^{(1)}$ [mΩ cm^2]	ΔR_t [mΩ cm^2]
Steam el. (1) (300 mA cm^{-2})	EC	22	1022	1000	440.4	527.7	87.3	292.2	306.9	14.7	732.6	834.6	102.0
Coel (300 mA cm^{-2})	EC	1055	1455	400	525.9	562.8	36.9	348.9	355.1	6.2	874.8	917.9	43.1
Coel (500 mA cm^{-2})	EC	1473	1673	200	541.4	555.2	13.8	261.0	259.0	−2.0	802.4	814.2	11.8
Steam el. (2) (300 mA cm^{-2})	EC	1701	2001	300	582.6	634.7	52.1	305.2	303.4	−1.8	887.8	938.1	50.3
EC/FC (300/−150 mA cm^{-2})	EC	2048	2312	264	593.8	602.2	8.4	323.6	295.8	−27.8	917.4	898.1	−19.3
	FC				584.9	615.1	30.2	653.1	664.6	11.5	1238.0	1279.7	41.7
Steam el. (3) (300 mA cm^{-2})	EC	2335	2635	300	638.8	709.8	71.0	305.7	314.7	9.0	944.6	1024.6	80.0

Table A.6

Resistance degradation rates derived from Table A.5. k^{full} is evaluated over the full phase duration, while k^{150} denotes the OLS slope over the final 150 h (see Fig. 4). For Phase 5, degradation rates are reported separately for EC and FC segments.

Phase	Mode	Δt [h]	k_s^{full} [mΩ cm^2 kh^{-1}]	k_s^{150} [mΩ cm^2 kh^{-1}]	k_p^{full} [mΩ cm^2 kh^{-1}]	k_p^{150} [mΩ cm^2 kh^{-1}]	k_t^{full} [mΩ cm^2 kh^{-1}]	k_t^{150} [mΩ cm^2 kh^{-1}]
Steam el. (1) (300 mA cm^{-2})	EC	1000	87.3	110.2 ± 1.3	14.7	−5.5 ± 1.6	102.0	104.7 ± 1.1
Coel (300 mA cm^{-2})	EC	400	92.2	78.7 ± 2.0	15.5	11.4 ± 4.3	107.8	90.1 ± 4.2
Coel (500 mA cm^{-2})	EC	200	69.0	65.7 ± 1.2	−10.0	−2.1 ± 1.5	59.0	63.6 ± 1.3
Steam el. (2) (300 mA cm^{-2})	EC	300	173.7	169.8 ± 1.3	−6.0	15.1 ± 1.5	167.7	184.8 ± 0.9
EC/FC (300/−150 mA cm^{-2})	EC	264	31.8	103.7 ± 3.2	−105.3	−23.1 ± 4.5	−73.1	80.5 ± 3.1
	FC		114.4	16.2 ± 30.6	43.6	46.0 ± 25.1	158.0	62.2 ± 9.9
Steam el. (3) (300 mA cm^{-2})	EC	300	236.7	232.3 ± 2.0	30.0	28.9 ± 2.7	266.7	261.2 ± 1.8

A.3. Validation of the neural DRT impedance reconstruction

In many DRT-based impedance studies the quality of the recovered distributions is judged mainly from the visual appearance of $G(\tau)$ and its qualitative consistency with expected processes, while the reconstruction accuracy with respect to the measured spectra is not quantified explicitly. In this work a stricter validation procedure is applied. For each spectrum the complex impedance is reconstructed from the recovered distribution $G(\tau)$, the fitted ohmic resistance R_s and the high-frequency inductance using the forward DRT integral model. Fig. A.9(a) compares the measured Nyquist curves (markers) with the neural DRT reconstructed curves (lines) for one representative spectrum from each operation phase. The agreement is very good for all investigated conditions and no systematic bias between measured and reconstructed arcs is visible.

The frequency-resolved reconstruction error is quantified in Fig. A.9(b) as

$$\|\Delta Z(f_k)\| = \sqrt{\left(Z'_{\mathrm{meas}}(f_k) - Z'_{\mathrm{rec}}(f_k)\right)^2 + \left(Z''_{\mathrm{meas}}(f_k) - Z''_{\mathrm{rec}}(f_k)\right)^2}$$

for each frequency point f_k. For the representative spectra the error remains well below 0.015 $\Omega\,\mathrm{cm}^2$ over most of the frequency range and increases only at the lowest frequencies where measurement noise and slow drift are most pronounced.

Fig. A.9(c) summarises the global distribution of $\|\Delta Z\|$ over all frequency points and all spectra. The median reconstruction error is 0.002 $\Omega\,\mathrm{cm}^2$, corresponding to approximately 0.251% of the median absolute impedance $|Z|$. The mean reconstruction error is 0.004 $\Omega\,\mathrm{cm}^2$ (about 0.580% of the mean $|Z|$). The 99th percentile reaches 0.042 $\Omega\,\mathrm{cm}^2$ due to a small number of low-frequency outliers. Typical Nyquist arc diameters in this dataset are on the order of 0.1 – 1 $\Omega\,\mathrm{cm}^2$, so the relative reconstruction error remains small for the vast majority of data points.

In addition, the recovered distributions $G(\tau, t)$ evolve smoothly over time in the DRT time-frequency maps, without unphysical frame-to-frame jumps or oscillatory artefacts. It is well known that multiple DRT distributions can reproduce a given impedance spectrum within the experimental noise level. The present neural DRT approach does not guarantee a unique solution, but it provides one stable and smooth solution that is comparable across all spectra in the data set. This comparability is essential for the subsequent degradation analysis, because changes in the extracted high-, mid- and low-frequency contributions can be interpreted as genuine trends rather than numerical artefacts.

A.4. Reference cell cross-section SEM

The reference cross-section is shown to document the as-received layer architecture and is not used for quantitative degradation conclusions.

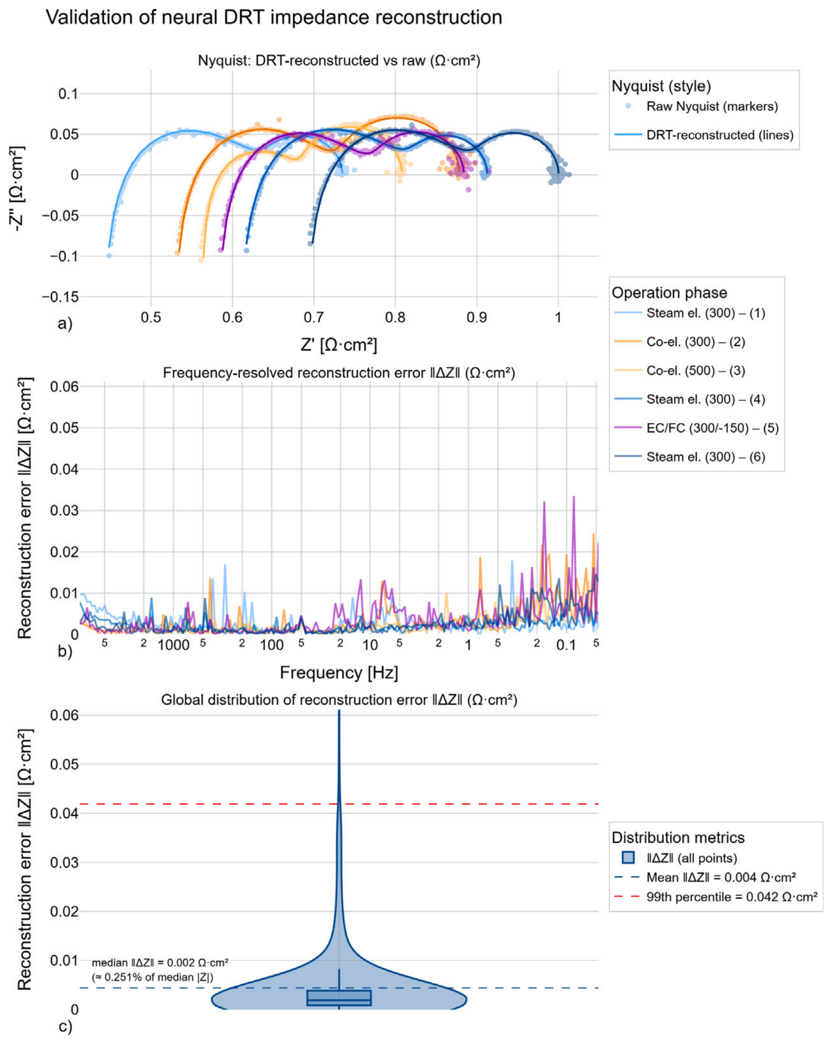

Fig. A.9. Validation of neural DRT solver impedance reconstruction. (a) Nyquist plots for one representative spectrum from each operation phase comparing raw data (markers) with neural DRT reconstructed curves (lines). (b) Frequency-resolved reconstruction error $\|\Delta Z\|$ for the same spectra. (c) Global distribution of $\|\Delta Z\|$ over all frequency points and spectra. The median reconstruction error is $0.002\,\Omega\,\mathrm{cm}^2$ (corresponding to $\approx$ 0.251% of the median $|Z|$), while the mean reconstruction error is $0.004\,\Omega\,\mathrm{cm}^2$ (about 0.580% of the mean $|Z|$).

A.5. EDX from cross-section SEM

Point EDX spectra were acquired at the locations marked in Fig. 8c (markers +1 and +2) of the BIB-polished cross-section, using the same SEM/EDX settings for each point. These spectra are provided for qualitative comparison only, to distinguish regions consistent with metallic Ni from regions consistent with locally oxidised Ni. No quantitative phase fraction is derived.

The supplier does not disclose the detailed barrier-layer composition. Therefore, area EDX spectra were recorded at the interlayer regions indicated in Fig. 8(b) and (d) to provide a qualitative compositional indication for both the fuel-side and air-side interfaces. Area spectra were selected to improve signal robustness for the thin interlayer and to reduce sensitivity to local microstructural heterogeneity. Identical SEM and EDX acquisition settings were applied to both locations to allow a direct qualitative comparison. The resulting spectra are shown in Fig. A.12. The spectra are qualitative and are not used to derive quantitative compositions or phase fractions.

A.6. DRT peak analysis

To make peak shifts explicit, Fig. A.13 shows the initial, after 24 h, and final DRT spectra for the same curves used in the EIS comparison. Peak positions were extracted for peak tracking by identifying local maxima of the DRT amplitude within predefined LF and HF frequency bands. Peak tracking was restricted to the measured frequency range ($f \leq f_{\max} \approx 10$ kHz) to avoid interpreting unconstrained behaviour outside the measurement bandwidth. In cases with multiple local maxima within a band, only the dominant maximum is reported in Table A.7, while secondary peaks remain visible in the spectra and are not used for quantitative tracking.

To support interpretation of peak movement, the DRT spectra in Fig. A.13 are complemented by peak tracking in Table A.7. Peaks are extracted as maxima of the DRT amplitude within predefined LF (1–100 Hz) and HF (1–10 kHz) frequency bands. If multiple local maxima occur within a band, only the dominant maximum is reported. The qualitative interpretation of these frequency regions follows the process-frequency overview reported in [7], which is intended as a guide rather than a strict mechanistic identification.

Data availability

Data will be made available on request.

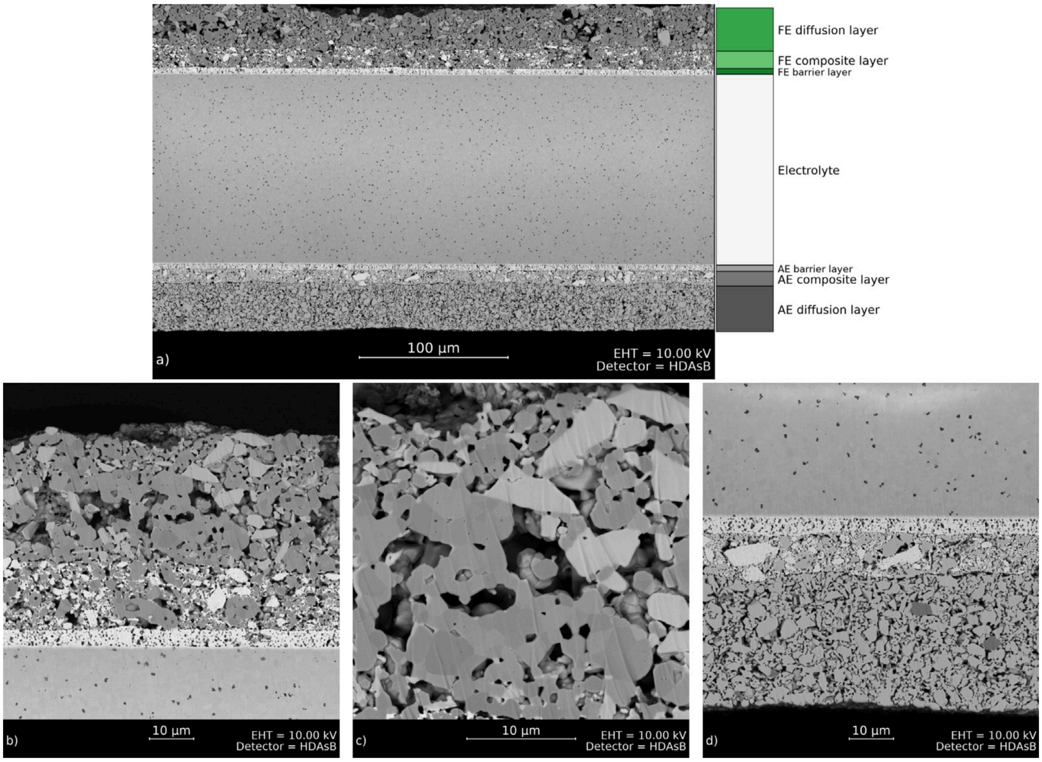

Fig. A.10. SEM cross-section of an unreduced reference cell. Panel (a) shows the full layer stack with labelled functional layers, barrier layers, and diffusion layers on fuel electrode and air electrode sides. Panels (b) to (d) show representative higher magnification views at identical magnification and field of view as used for the post-test cross-section images to enable direct comparison. All subpanels were assembled and annotated using the same processing script and layout convention as the post-test cross-section figure.

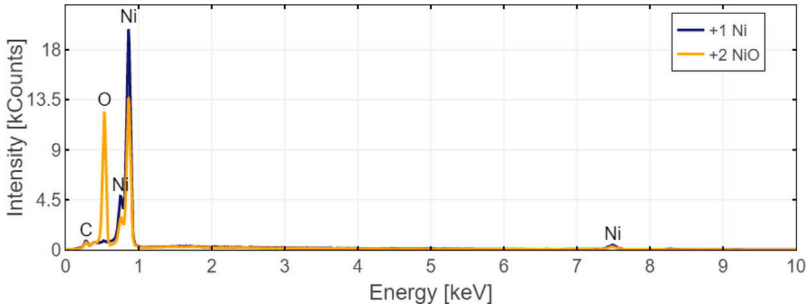

Fig. A.11. EDX spectra acquired at the marked cross-section locations in Fig. 8c to qualitatively distinguish metallic and oxidised Ni regions. Spectrum +1 is Ni-rich and dominated by Ni peaks, whereas spectrum +2 shows a pronounced oxygen peak (around 0.52 keV) in addition to Ni, consistent with NiO. The spectra are provided for qualitative comparison and no quantitative phase fraction is derived.

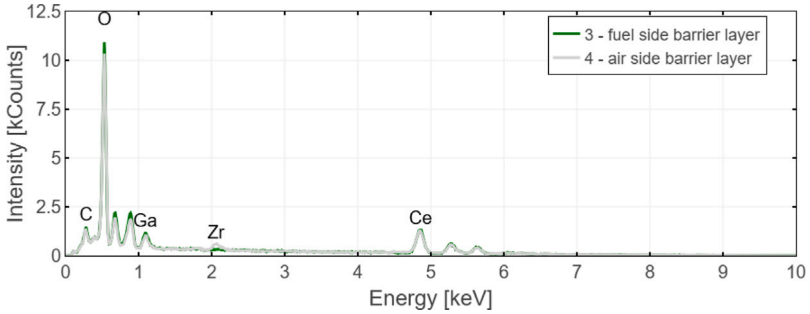

Fig. A.12. Qualitative EDX spectra acquired at the marked interlayer (barrier-layer) regions at the fuel-side (Spectrum 3) and air-side (Spectrum 4) electrolyte interfaces as indicated in Fig. 8. Both spectra show pronounced Ce peaks, indicating a ceria-containing interlayer on both sides. A Ga signal is also observed in the interlayer region. The spectra are provided for qualitative comparison only and no quantitative composition or phase fraction is derived.

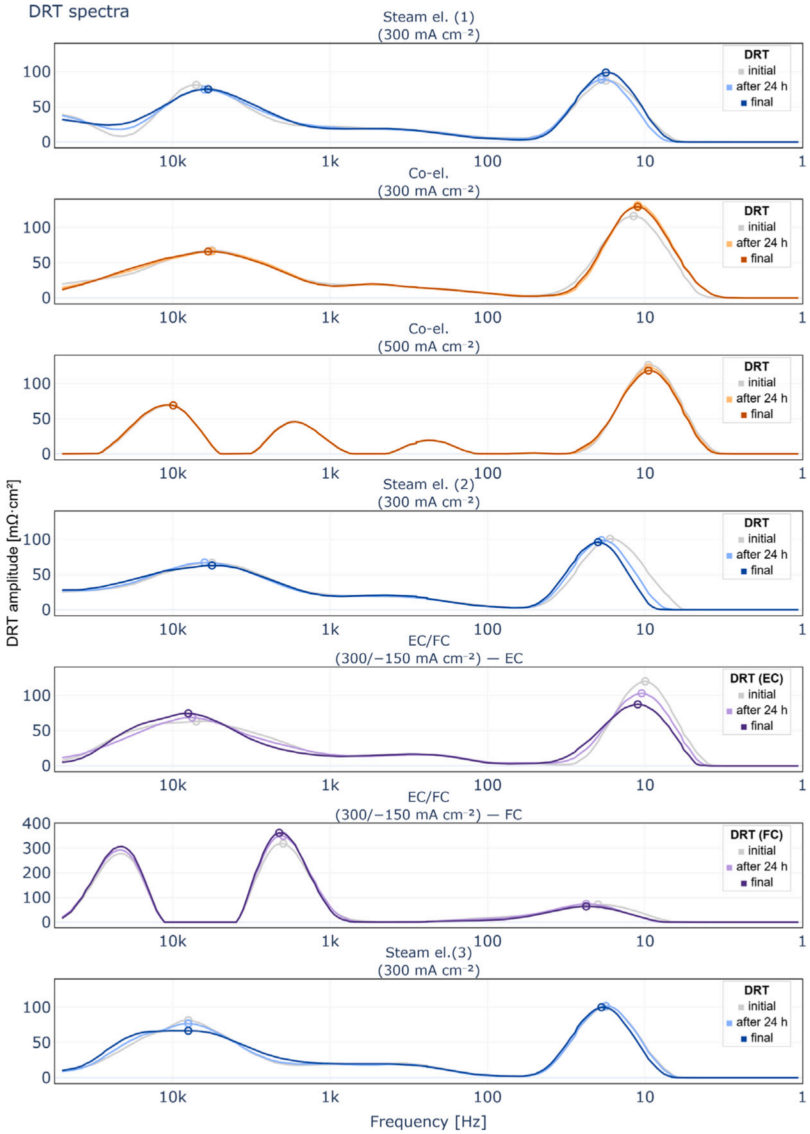

Fig. A.13. DRT spectra for the same impedance curves used in the phase-resolved EIS comparison (initial, ~24 h, final). Circle markers indicate the extracted LF and HF peak maxima used for peak tracking in Table A.7. Frequency-process interpretation follows the guideline overview in [7]. Minor oscillations close to the frequency boundaries are inversion artefacts and are not interpreted. Note the different *y*-axis scale in the FC panel.

Table A.7
Low-frequency (LF) and high-frequency (HF) DRT peak positions and amplitudes for the curves shown in Fig. A.13 (initial, ~24 h, final). Peaks are extracted as maxima of the DRT amplitude within two operational frequency windows (LF: 1–100 Hz, HF: 1–10 kHz). Where multiple local maxima occur within a window, only the dominant maximum is reported for peak tracking. Frequency-process interpretation follows the guideline overview in [7].

Section	Curve	f_{LF} [Hz]	A_{LF} [mΩ cm^2]	f_{HF} [Hz]	A_{HF} [mΩ cm^2]
Steam el. (1) (300 mA cm^{-2})	initial	17.7	87.2	7079.9	81.1
	~24 h	18.9	89.0	6272.3	74.6
	final	17.7	98.8	5947.1	75.1
Coel (300 mA cm^{-2})	initial	11.8	116.3	5622.7	67.8
	~24 h	11.1	131.9	5622.7	66.4
	final	11.1	129.5	5947.1	66.0
Coel (500 mA cm^{-2})	initial	9.5	126.3	9911.9	68.5
	~24 h	9.5	122.4	9911.9	69.1
	final	9.5	118.4	9911.9	69.1
Steam el. (2) (300 mA cm^{-2})	initial	16.7	100.8	5622.7	66.9
	~24 h	18.9	98.9	6272.3	67.3
	final	19.8	96.2	5622.7	63.1

(*continued on next page*)

Table A.7 (*continued*).

EC/FC (300/−150 mA cm^{-2}) — EC	initial	10.0	120.1	7079.9	63.1
	∼24 h	10.5	103.2	7502.0	68.7
	final	11.1	87.3	7952.2	74.5
EC/FC (300/−150 mA cm^{-2}) — FC	initial	19.8	71.3	1982.4	318.8
	∼24 h	23.6	73.4	1982.4	349.8
	final	23.6	64.1	2103.7	362.5
Steam el. (3) (300 mA cm^{-2})	initial	17.7	101.0	7952.2	81.7
	∼24 h	17.7	101.9	7952.2	77.2
	final	18.9	100.1	7952.2	66.8

References

[1] Intergovernmental Panel on Climate Change (IPCC), Climate Change 2023: Synthesis Report. Contribution of Working Groups I, II and III to the Sixth Assessment Report of the Intergovernmental Panel on Climate Change, Intergovernmental Panel on Climate Change, Geneva, Switzerland, 2023, http://dx.doi.org/10.59327/IPCC/AR6-9789291691647, URL http://dx.doi.org/10.59327/IPCC/AR6-9789291691647.

[2] S. Dermühl, U. Riedel, A comparison of the most promising low-carbon hydrogen production technologies, Fuel 340 (2023) 127478, http://dx.doi.org/10.1016/J.FUEL.2023.127478.

[3] Y. Zheng, Z. Chen, J. Zhang, Solid oxide electrolysis of H2O and CO2 to produce hydrogen and low-carbon fuels, Electrochem. Energy Rev. 4 (3) (2021) 508–517, http://dx.doi.org/10.1007/s41918-021-00097-4.

[4] J. Peacock, R. Cooper, N. Waller, G. Richardson, Decarbonising aviation at scale through synthesis of sustainable e-fuel: A techno-economic assessment, Int. J. Hydrog. Energy 50 (2024) 869–890, http://dx.doi.org/10.1016/j.ijhydene.2023.09.094.

[5] T.L. Cheng, Y. Lei, Y. Chen, Y. Fan, H. Abernathy, X. Song, Y.H. Wen, Oxidation of nickel in solid oxide cells during electrochemical operation: Experimental evidence, theoretical analysis, and an alternative hypothesis on the nickel migration, J. Power Sources 569 (2023) 232991, http://dx.doi.org/10.1016/J.JPOWSOUR.2023.232991.

[6] F. Mütter, P. Boškoski, S. Megel, C. Hochenauer, V. Subotić, Optimising solid oxide cells for co-electrolysis operation: parameter interactions and efficiency gains at industrial scale, Appl. Energy 396 (2025) 126229, http://dx.doi.org/10.1016/j.apenergy.2025.126229.

[7] F. Mütter, P. Boškoski, S. Megel, C. Hochenauer, V. Subotić, Operating sensitivities for steam versus co-electrolysis on a commercial solid-oxide electrolysis stack with Power-to-X implications, Fuel 411 (2026) 137992, http://dx.doi.org/10.1016/J.FUEL.2025.137992.

[8] F. Tietz, D. Sebold, A. Brisse, J. Schefold, Degradation phenomena in a solid oxide electrolysis cell after 9000 h of operation, J. Power Sources 223 (2013) 129–135, http://dx.doi.org/10.1016/j.jpowsour.2012.09.061.

[9] J. Schefold, A. Brisse, H. Poepke, 23,000 h steam electrolysis with an electrolyte supported solid oxide cell, Int. J. Hydrog. Energy 42 (19) (2017) 13415–13426, http://dx.doi.org/10.1016/J.IJHYDENE.2017.01.072.

[10] M. Lang, S. Raab, M.S. Lemcke, C. Bohn, M. Pysik, Long-term behavior of a solid oxide electrolyzer (SOEC) stack, Fuel Cells 20 (6) (2020) 690–700, http://dx.doi.org/10.1002/fuce.201900245.

[11] Q. Shao, D. Jin, Y. Lu, Y. Yu, L. Luo, X. Sun, C. Guan, J.Q. Wang, Performance evolution analysis of solid oxide electrolysis cells operating at high current densities, Int. J. Hydrog. Energy 57 (2024) 709–716, http://dx.doi.org/10.1016/j.ijhydene.2024.01.096.

[12] Y. Tao, S.D. Ebbesen, M.B. Mogensen, Degradation of solid oxide cells during co-electrolysis of steam and carbon dioxide at high current densities, J. Power Sources 328 (2016) 452–462, http://dx.doi.org/10.1016/J.JPOWSOUR.2016.08.055.

[13] M. Rao, X. Sun, A. Hagen, Durability of solid oxide electrolysis stack under dynamic load cycling for syngas production, J. Power Sources 451 (2020) 227781, http://dx.doi.org/10.1016/J.JPOWSOUR.2020.227781.

[14] N. Trofimenko, M. Kusnezoff, A. Michaelis, Optimization of ESC performance for co-electrolysis operation, ECS Trans. 78 (1) (2017) 3025–3037, http://dx.doi.org/10.1149/07801.3025ECST/XML.

[15] V.N. Nguyen, Q. Fang, U. Packbier, L. Blum, Long-term tests of a Jülich planar short stack with reversible solid oxide cells in both fuel cell and electrolysis modes, Int. J. Hydrog. Energy 38 (11) (2013) 4281–4290, http://dx.doi.org/10.1016/J.IJHYDENE.2013.01.192.

[16] S.E. Wolf, V. Vibhu, E. Tröster, I.C. Vinke, R.A. Eichel, L.G. de Haart, Steam electrolysis vs. Co-electrolysis: Mechanistic studies of long-term solid oxide electrolysis cells, Energies 15 (15) (2022) 5449, http://dx.doi.org/10.3390/EN15155449/S1.

[17] J. Liu, F. Ciucci, The deep-prior distribution of relaxation times, J. Electrochem. Soc. 167 (2) (2020) 026506, http://dx.doi.org/10.1149/1945-7111/ab631a.

[18] D. Reiner, S.a. Marković, H. Schröttner, C. Hochenauer, V. Subotić, Electrochemical investigation of the influence of gas compositions on industrial-sized fuel electrode supported single cells under co- and CO2-electrolysis conditions, J. CO2 Util. 99 (2025) 103152, http://dx.doi.org/10.1016/J.JCOU.2025.103152.

[19] Q. Fang, C.E. Frey, N.H. Menzler, L. Blum, Electrochemical performance and preliminary post-mortem analysis of a solid oxide cell stack with 20,000 h of operation, J. Electrochem. Soc. 165 (2) (2018) F38–F45, http://dx.doi.org/10.1149/2.0541802JES/XML.

[20] S. Nuggehalli Sampathkumar, P. Aubin, K. Couturier, X. Sun, B.R. Sudireddy, S. Diethelm, M. Pérez-Fortes, J. Van herle, Degradation study of a reversible solid oxide cell (rSOC) short stack using distribution of relaxation times (DRT) analysis, Int. J. Hydrog. Energy 47 (18) (2022) 10175–10193, http://dx.doi.org/10.1016/j.ijhydene.2022.01.104.

[21] M. Lang, Y.S. Lee, I.S. Lee, P. Szabo, J. Hong, J. Cho, R. Costa, Analysis of electrochemical degradation phenomena of a 60-cell SOC stack operated in reversible SOFC/SOEC cycling mode, Appl. Energy 386 (2025) 125565, http://dx.doi.org/10.1016/j.apenergy.2025.125565.

[22] X. Sun, P.V. Hendriksen, M.B. Mogensen, M. Chen, Degradation in solid oxide electrolysis cells during long term testing, Fuel Cells 19 (6) (2019) 740–747, http://dx.doi.org/10.1002/FUCE.201900081.

[23] L.N. Smith, Cyclical learning rates for training neural networks, in: Proceedings - 2017 IEEE Winter Conference on Applications of Computer Vision, WACV 2017, 2017, pp. 464–472, http://dx.doi.org/10.1109/WACV.2017.58, arXiv:1506.01186.